Probabilistic space- and time-interaction modeling of main-shock earthquake rupture occurrence

Luis Ceferino[1], Anne Kiremidjian[1], and Gregory Deierlein[1]

[1]Civil and Environmental Engineering Department, Stanford University

April 29, 2019

Abstract

This paper presents a probabilistic formulation for modeling earthquake rupture processes of mainshocks. A correlated multivariate Bernoulli distribution is used to model rupture occurrence. The model captures time interaction through the use of Brownian passage-time (BPT) distributions to assess rupture interarrival in multiple sections of the fault, and it also considers spatial interaction through the use of spatial correlograms. The correlograms represents the effect of rupture nucleation and propagation. This model is proposed as an attractive alternative to existing probabilistic models because it (1) incorporates time and space interactions of mainshocks, (2) preserves the marginal distributions of interarrival times after including spatial rupture interactions (i.e., model consistency), and (3) has an implicit physical interpretation aligned with recent rupture behavior observations. The proposed model is applied to assess the occurrence of large interface earthquakes in the subduction zone along the Coast of Lima, Peru. The model matches both the annual magnitude exceedance rates and the average seismic moment release in the tectonic region. Time-dependent seismic hazard in the region is also calculated, and the results demonstrate that by accounting for recent earthquake occurrences, the inclusion of time-dependent effects can reduce the 30-year seismic hazard by a factor of four.

1 Introduction

Modeling of earthquake rupture occurrence is one of the most important components of earthquake hazard analysis, which underlies Performance-based Earthquake Engineering (PBEE) and earthquake risk assessments. Earthquake rupture modeling remains a particular challenge due to limited data and knowledge to reliable characterize earthquake ruptures. As a result, probabilistic hazard analyses employ multiple simplifying assumptions to account for the interactions between earthquake arrival, location, rupture size, and magnitude.

Two main approaches are used to model earthquake rupture, physics-based and probabilistic. Physics-based theories have been proposed to explain the underlying mechanics of earthquakes. The elastic rebound theory, first proposed by Reid (1911), describes earthquake ruptures as the result of the sudden releases of elastic strain, which is slowly accumulated through interseismic cycles. Though the elastic rebound theory only provides a conceptual description of the nature of earthquake cycles, it has been the theoretical basis behind more modern, quantitative earthquake theories. Recently, modern rock fracture models and efficient computational tools have allowed physics-based simulations of earthquake rupture cycles (e.g., Luo et al. (2017); Richards-Dinger and Dieterich (2012)). At the present, the rate and state friction law (Dieterich (1979); Ruina (1983); Marone (1998)) is the canonical model for simulating such cycles. Applications of the state and friction law have allowed researchers to reproduce complex fault rheologies and earthquake rupture behaviors such as nucleation (e.g., Galvez et al. (2014)), earthquake swarms (e.g., Lohman and McGuire (2007)), aftershocks (e.g., Dieterich (1994)), postseismic relaxation (e.g., Savage and Langbein (2008)), and coseismic, interseismic and postseismic strain and stress cycles (e.g., Barbot et al. (2012)). While physics-based models are conceptually attractive, they are highly computationally intensive and depend on multiple unobserved fault parameters (e.g., fault normal stresses, constitutive law parameters, fault asperities). These parameters are uncertain, and as a result, propagation of these uncertainties needs to be considered when the seismic hazard is computed. Propagation of parameter uncertainty is extremely challenging due to current computational constraints and to the large sensitivity of the model results to such uncertainties.

Probabilistic formulations for earthquake rupture occurrence have been extensively used for modeling earthquake hazard due to their relative simplicity compared to physics-based formulations. Moreover, these models are observational data-driven and allow for direct incorporation of uncertainty of rupture occurrence. Researchers have proposed several probabilistic models that vary in corresponding physical interpretation, complexity level, and assumed physical interactions over the fault space, rupture inter-arrival, and earthquake size and magnitude. In spite of their maturity, probabilistic formulations for rupture modeling remain an active line of research because existing models (1) do not fully describe interactions of earthquake rupture over fault space, earthquake arrival, magnitude, and rupture size, (2) have significantly less correspondence to the modern earthquake rupture theories than the existing physics-based methodologies, or (3) lack probabilistic model consistency (i.e., mismatch between the assumed and simulated distribution of rupture interarrival times in the fault, e.g., Field (2015)). This paper presents a new probabilistic formulation for modeling earthquake rupture occurrence of mainshocks by explicitly capturing the modeling of rupture interactions over time and space. Though this formulation does not fully resolve all the modeling issues described above, it provides concrete steps forward in probabilistic rupture modeling by (1) including the modeling of key rupture interactions, (2) detailing the physical interpretation of the model, and (3) demonstrating the consistency of the model both analitically and through simulation.

The paper begins with a brief summary of existing probabilistic models. Then, it describes the proposed probabilistic model including the model's physical interpretation. Next, it provides a case study to showcase (1) the applicability of the proposed model and the parameter estimation techniques to replicate earthquake occurrence of large interface ruptures occurring on the subduction fault along the Coast of Lima, Peru; (2) benchmarking of the model performance against historical magnitude exceedance rates and spatial distribution of average seismic moment release; and (3) a comparison of time-dependent earthquake hazard estimations based on the proposed model and time-independent hazard assessments. A mathematical proof of the theoretical consistency of the model is included in an appendix.

2 Existing models for Earthquake rupture process modeling

Several probabilistic formulations have been proposed to model earthquake rupture occurrence based on either empirical observations or theories of earthquake rupture interactions on seismic faults. The following briefly summarizes four categories of these models.

2.1 Time-independent models

The Poisson model is a time-independent model and is arguably the most frequently used probabilistic model (e.g., seismic hazard data for building codes (Petersen et al. (2014)) given its simplicity in modeling tectonic plate interactions. The canonical Poisson model is homogeneous over a seismic fault, which means that ruptures are equally likely at every point of the fault. Another characteristic of the Poisson model is that the hazard rate, defined as the instantaneous likelihood of earthquake occurrence, is independent of previous earthquakes. This contradicts the elastic rebound theory since it ignores the time-dependent build-up and release of tectonic strains between earthquakes.

2.2 Time-interaction models

Time-interaction models are one that incorporate the earthquake occurrence intervals of characteristic earthquakes. According to the characteristic earthquake theory, seismic faults tend to generate almost the same large rupture with a magnitude in a relatively narrow range close to the maximum (Schwartz and Coppersmith (1984); Wesnousky (1994)). Additionally, the earthquake interarrival time (i.e., time between subsequent earthquakes) is modeled uncoupled and independent from the rupture magnitude. Probability distributions for earthquake interarrival time included Gaussian (Rikitake (1974)), Weibull (Hagiwara (1974)), Lognormal (Nishenko and Buland (1987)), Gamma (Udias and Rice (1975)), and the Brownian passage-time distribution (BPT) (Kagan and Knopoff (1987); Matthews et al. (2002)). All these models capture the sudden drop of probability of earthquake occurrence immediately after the occurrence of a preceding earthquake. They also capture the probability increase over time as the slip re-accumulates in the seismic fault. These model features correspond to the earthquake behavior described by the elastic-rebound theory. Matthews et al. (2002) performed a thorough comparison among the implied earthquake arrival behavior of the models and developed corresponding mathematical expressions for the their impact on the earthquake hazard rates. Thus, these models capture important characteristics of rupture data, which is consistent with the elastic-rebound theory. In particular, the BPT distribution provides an explicit physics-based representation of the rupture process. As stated by Matthews et al. (2002), the BPT models earthquake ruptures as sudden releases of tectonic stress, which accumulates over interseismic cycles and has a random component.

2.3 Time- and magnitude-interaction models

Time- and magnitude-interaction models are the ones that consider the coupling between the earthquake interarrival time and magnitude. These models built on the slip-predictable and time-predictable hypotheses. The slip-predictable model (Kiremidjian and Anagnos (1984)) assesses the earthquake interarrival time using one of the time-interaction models described above, and introduces a magnitude function that increases based on the time since the last earthquake. The time-predictable model (Anagnos and Kiremidjian (1984)), on the other hand, assesses the interarrival time with a probabilistic model that is function of the magnitude of the last earthquake. In this model, large earthquake ruptures induce long waiting times for the next earthquake. Even though these models incorporate coupling between the interarrival time and the earthquake magnitude, they do not address the uncertainty and the spatial dependencies originated from earthquake ruptures occurring at different locations of the seismic faults.

2.4 Space- and time-interaction models

There are few probabilistic models that have incorporated both the spatial and the time dependencies of earthquake rupture processes. Lutz and Kiremidjian (1995) proposed a model including these dependencies using a generalized Semi-Markov process. The model discretizes the fault into small sections

and evaluates earthquake cycles by (1) selecting the nucleation point according to accumulated slip distribution in the fault sections, (2) estimating the rupture length based on the accumulated slip at the nucleation section, and (3) propagating the rupture to corresponding neighboring sections.

Subsequently, the Uniform California Earthquake Rupture Forecast version 2 (UCERF v2) proposed a different approach composed of two main steps. First, the occurrence probabilities of all possible earthquake ruptures in the discretized fault system are computed using a combination of BPT distributions that incorporate information on the last rupture time in different fault locations (Field and Gupta (2008)). Next, all the rupture occurrences are sampled independently and then combined to estimate the time-dependent seismic hazard. Observations from the model application showed a mismatch between the assumed BPT distributions and the resultant simulated distributions of rupture interarrival times (see Figure 2, 5, and 6 in Field and Gupta (2008)). This issue will be referred as lack of model "consistency" hereafter. The UCERF version 3 (UCERF v3) improved the consistency of the model, but it did not achieve full consistency (Field (2015)).

Other methodologies have used smoothed seismicity for modeling interaction of time, space, and magnitude of earthquake ruptures. Smoothed seismicity models assume that the seismicity rates are the sum of two components: the background seismicity (often heterogeneous in space and stationary in time) and triggered events (e.g., aftershocks) (Kagan and Knopoff (1987); Ogata (1988); Marsan and Lengliné (2008)). Smoothed seismicity models are constructed through kernels (i.e., window functions) that capture variations of seismicity rates over large regions by smoothing the past earthquake locations to infer the spatial distribution of future earthquakes. For example, existing smoothed seismicity models have been proposed to forecast worldwide earthquake rates as a function of location, magnitude, and focal mechanism (Kagan and Jackson (2014, 2015)). Because the background seismicity is stationary in time, the smoothed seismicity models do not account for interactions of mainshocks over time, and they only can account for triggered events (i.e., aftershocks). Recently, Helmstetter and Werner (2014) proposed a purely data-driven smoothed seismicity model incorporating such spatiotemporal interactions. The model fitted the seismicity data well and gave similar results to those obtained with other more complex models such us the epidemic-type aftershock sequence (ETAS) (Ogata (1988)).

The model presented in this paper captures spatiotemporal interactions of earthquake mainshocks in tectonic regions and represents an alternative to other existing methodologies. Therefore, this paper does not provide such comparisons. The model incorporates three characteristics that are relevant for rupture simulation. (1) The model captures spatiotemporal interactions of mainshocks unlike current smoothed seismicity models. (2) The model assumed and simulated distributions of rupture interarrival times are shown to be consistent, in contrast to other approaches such as the UCERF model. (3) The model has an implicit physical interpretation compatible with modern earthquake rupture theories. The next sections describe the proposed model, parameter estimation techniques, and the physical interpretation of the model.

3 Probabilistic model formulation

The model presented here is the 2-D extension of the 1-D probabilistic rupture model presented by Ceferino et al. (2017). The 1-D probabilistic model was built to assess the spatial and temporal interactions of earthquake mainshock occurrences. The model is based on the fundamental premise of the elastic rebound theory, which states that earthquakes are the result of cyclic processes characterized by accumulation of strain and stress over time in a tectonic fault that are released through earthquake ruptures. It follows from this theory that the likelihood of occurrence of new mainshock greatly decreases after the occurrence of such an event and increases as time since the last rupture increases.

3.1 Notation and representation of the fault and ruptures

The model represents the surface of contact (i.e., interface) between tectonic plates as an area that is discretized into small sections as shown in Figure 1. These sections represent the smallest area that can be ruptured in the model. Figure 1 shows the sections with ruptures occurring at time t as shaded areas.
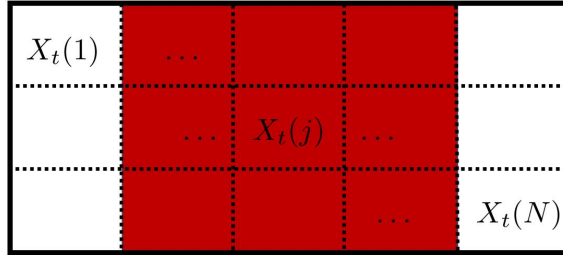
Figure 1: Fault discretization into N small sections. The shaded sections represent a rupture on the fault at time t.

Similar to the 1-D version of the model (Ceferino et al. (2017)), X_t is the rupture vector at year t, where $X_t \in \{0,1\}^N$. N is the total number of fault sections and t is the time index, which is defined to have time steps of one year. Each element of the vector X_t, shown in Figure 1, is denoted by $X_t(j)$ and represents the rupture state of the j-th section of the fault. $X_t(j)$ is equal to 1 if there is a rupture during year t and 0 otherwise, for $j = 1, 2, \cdots, N$. Ruptures of multiple adjacent sections in a given year t are assumed to be generated by a single large earthquake event, and ruptures of non-adjacent sections in year t are assumed to be generated by multiple earthquake events. In addition, T_t is defined as the vector of the times since the last earthquake until year t for each section, where $T_t \in \mathbb{N}^N$. $T_t(j)$ is the j-th element of the vector T_t corresponding to the time since the last earthquake in the j-th section, where $j = 1, 2, \cdots N$. Thus, at the next one-year time step: $T_{t+1}(j)$ will either equal $T_t(j) + 1$ if there was no rupture in the j-th section during year t (i.e., $X_t(j) = 0$), or reset to one if there was a rupture (i.e. $X_t(j) = 1$). This relationship is represented in Equation 1.

$$T_{t+1}(j) = (T_t(j))(1 - X_t(j)) + 1 \tag{1}$$

3.2 Model description

The earthquake rupture X_t at time t conditioned on the time since the last rupture T_t is modeled as a multivariate Bernoulli distribution as shown in Equation 2. The rupture occurrence marginal probabilities are defined by the vector p_t, which is based on a correlation model that is explained later in the paper. The vector p_t has N elements $p_t(j)$, where $p_t(j)$ is function of the time since the last rupture $T_t(j)$ at the j-th section. $p_t(j)$ can be estimated as in Equation 3, where τ_j is a random variable that represents the the rupture interarrival time of the j-th section. Then, $p_t(j)$ is the annual rupture probability (i.e., rupture rate) of the j-th section.

$$X_t | T_t \sim \text{Mutivariate Bernoulli}(p_t) \tag{2}$$

$$p_t(j) = P[X_t(j) = 1 | T_t(j)] = P[\tau_j \leq T_t(j) | \tau_j > T_t(j) - 1] = \frac{P[T_t(j) - 1 < \tau_j \leq T_t(j)]}{1 - P[\tau_j \leq T_t(j) - 1]} \tag{3}$$

The interarrival time τ_j is modeled as a Brownian passage-time (BPT) probability distribution, also known as Inverse Gaussian distribution. The model can also take other distributions (e.g., Lognormal Nishenko and Buland (1987), Gamma (Udias and Rice (1975)), Weibull (Hagiwara (1974))). The model extends the point-source version of the BPT distribution proposed by Matthews et al. (2002) by representing multiple sections of a discretized tectonic fault through the correlated Bernoulli distribution of Equation 2. The BPT model has been widely used in research and applications (e.g. Time-dependent California seismic hazard by Field (2015)). Matthews et al. (2002) gives a comprehensive description of the analysis and applicability of this distribution for modeling earthquake rupture occurrence.

The BPT probability density function (pdf) for τ_j is given in Equation 4. A comprehensive description of the statistical properties of the BPT distribution are provided in Tweedie (1957); Chhikara and Folks (1977). The BPT distribution is defined by the parameters μ_j (mean interarrival time) and α_j (aperiodicity or coefficient of variation). The cumulative distribution function (CDF) of the BPT distribution is given in Equation 5, where Φ is the standard normal CDF. Using Equations 3 and 5, $p_t(j)$ can be rewritten as in Equation 6. The case study presented in the next section provides descriptions of $p_t(j)$ and the BPT distribution.

$$f_{\tau_j}(t) = \Big(\frac{\mu_j}{2\pi\alpha_j t^3}\Big)^{1/2} \exp\Big(-\frac{(t-\mu_j)^2}{2\mu_j\alpha_j^2 t}\Big) \tag{4}$$

$$F_{\tau_j}(t) = P[\tau_j \leq t] = \Phi[u_1(t)] + e^{2/\alpha_j^2}\Phi[-u_2(t)] \tag{5a}$$

$$u_1(t) = \alpha_j^{-1}[t^{1/2}\mu_j^{-1/2} - t^{-1/2}\mu_j^{1/2}] \tag{5b}$$

$$u_2(t) = \alpha_j^{-1}[t^{1/2}\mu_j^{-1/2} + t^{-1/2}\mu_j^{1/2}] \tag{5c}$$

$$p_t(j) = \frac{(\Phi[u_1(T_t(j))] - \Phi[u_1(T_t(j)-1)]) + e^{2/\alpha_j^2}(\Phi[-u_2(T_t(j))] - \Phi[-u_2(T_t(j)-1)])}{1 - (\Phi[u_1(T_t(j)-1)] + e^{2/\alpha_j^2}\Phi[-u_2(T_t(j)-1)])} \tag{6}$$

Spatial rupture correlations are introduced represent the influence that a rupture at one section has on triggering a rupture on neighboring sections. In other words, it represents the spatial propagation effect of earthquake ruptures. The correlation is introduced through a correlogram function. Two correlogram functions are evaluated in this paper, the exponential and spherical correlograms. Their respective formulas are given by Equations 7 and 8. These functions output the correlation of rupture occurrence $X_t(i)$ and $X_t(j)$ between the sections i and j at any time t. The correlation is considered constant over time. The exponential correlogram decays as a function of the distance $dist(i,j)$ between the i-th and j-th sections, whereas the spherical correlogram decays as a function of the square of that normalized distance. The parameter γ defines the rate at which the correlation decays with distance.

$$\rho_{i,j} = \exp\Big(-\frac{dist(i,j)}{\gamma}\Big) \tag{7}$$

$$\rho_{i,j} = \exp\Big(-\Big(\frac{dist(i,j)}{\gamma}\Big)^2\Big) \tag{8}$$

3.3 Approximation through Copula

Given the probabilities $p_t(j)$ and correlations $\rho_{i,j}$ of rupture occurrence, the annual rupture occurrence can be estimated using the correlated multivariate Bernoulli distribution. However, this distribution cannot be written in close-form solution, and therefore sampling from the "true" multivariate correlated Bernoulli distribution becomes infeasible. To overcome this issue, the copula method is used, which provides an approximation to the multivariate Bernoulli (Jin et al. (2015)). First, a vector Z_t of normally distributed random variables is defined. The mean of Z_t is a zero-valued vector, and the covariance is represented by the covariance matrix of $X_t|T_t$, whose values come from the correlogram either in Equation 7 or 8). Then, $X_t(j)$ is obtained by evaluating whether $\Phi[Z_t(j)]$ is smaller than $p_t(j)$ as in Equation 9, where $Z_t(j)$ is the j-th element of the vector Z_t. Because the copula method is approximate, the final spatial correlations of rupture occurrence will be different from the correlation model in Equation 7 or 8. The case study in the paper shows the comparisons between the correlation values from the correlogram models in Equations 7 and 8 and the effective correlations resulting from simulations after applying the copulas method.

$$X_t(j) = \mathbf{1}\{\Phi(Z_t(j)) < p_t(j)\} \tag{9}$$

3.4 Physical interpretation of the model

The probability distribution of the rupture interarrival time defines the rupture process at each fault section. This model uses a BPT distribution for interarrival times because it has a direct underlying physical interpretation of the rupture process. Matthews et al. (2002) described that the BPT distribution models the time of failure occurrence of a Brownian Relaxation Oscillator (BRO). In addition, Matthews et al. (2002) interpreted that the BRO behaves as an earthquake rupture process with a load that has two additive components: one represents an increasing load with constant rate, and the other represents a (random) Brownian perturbation. Each time the load hits a fixed threshold, it resets to initial conditions. The "load" in the BRO can represent the accumulated tectonic strain that is released after reaching a strain threshold or the accumulated tectonic shear stress that is released upon reaching a Coulomb stress threshold. Both interpretations represent the earthquake mechanics described in the elastic rebound theory. A direct implication of the BPT and BRO is that the stress gains and seismic gaps can increase the likelihood of rupture occurrence. Existing studies have found evidence supporting this implication; for example, Strader and Jackson (2014); Strader et al. (2015) observed that the accumulated static Coulomb stress can indicate future earthquake locations.

Figure 2 illustrates the behavior of a BRO over 500 years. The load threshold was set to 100 load units, with a fixed rate of 1 load unit per year and a Brownian motion with standard deviation of 7. Each time the load reaches 100, it resets to 0. The rupture interarrival time (i.e., time difference between two consecutive threshold hitting times) of this BRO is distributed as a BPT with a μ_j of 100 years and a α_j of 0.7. Similar values of μ_j and α_j were found in the application presented later in this paper. A μ_j of 100 years means that the BRO will reach the threshold on average every 100 years. The aperiodicity α_j is directly related to the standard deviation (i.e., weight) of the random perturbation in the load path. A 0-valued aperiodicity would imply a fully periodic rupture interarrival (i.e., the time between ruptures would be constant).
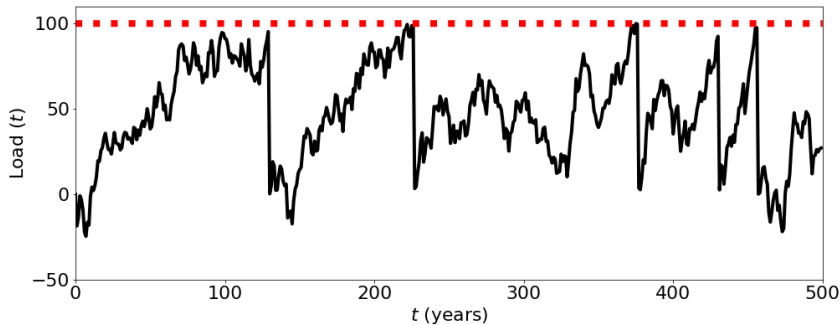

Figure 2: Realizations of load path in Brownian motion for constant μ (100 years) and different values of α (aperiodicity).

The BRO and BPT represent the rupture cycle of each section of the fault, each of which has specific values of mean interarrival μ_j and aperiodicity α_j. In the model, these BRO's can reach failure simultaneously triggering larger earthquakes (i.e., involving multiple sections). The spatial interactions among the BROs at different sections are modeled through a spatial correlation law (e.g., exponential or spherical correlogram). The correlogram introduces an interaction among the stress paths and increases the likelihood of having several neighboring sections reach their respective stress thresholds simultaneously. Figure 3 shows a conceptual representation of three BRO stress paths. The sections can reach failure separately as shown at time t_1 and t_2, or fail simultaneously as at time t_3. The correlation decays with distance in our model; therefore, sections that are at large distances have weak correlation with each other. This model feature can represent the process of rupture nucleation and propagation during large

earthquakes since the rupture in one section of the fault can trigger the rupture of neighboring areas of the fault (e.g., Ellsworth and Beroza (1995)).
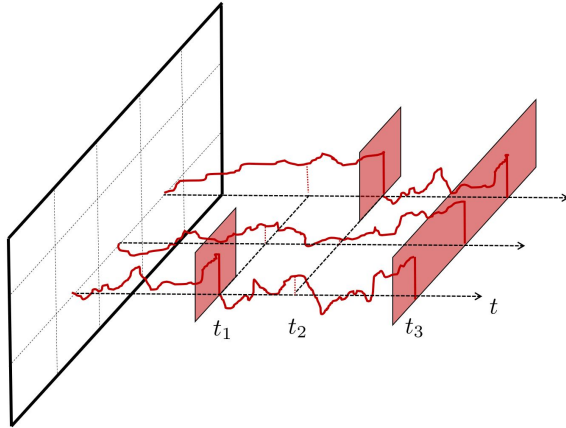

Figure 3: Conceptual representation of stress paths and simultaneous ruptures.

3.5 Consistency of the model

As previously mentioned, some probabilistic models that capture rupture interactions over space and time (e.g., UCERF v2 and UCERF v3) have what are referred to as "consistency" issues. This means that there is a mismatch between the assumed probability distribution of earthquake interarrival time and the resultant distribution from the simulation of earthquake ruptures on a fault (see Field and Gupta (2008); Field (2015)). The proposed model preserves the probability distribution of earthquake interarrival time at each section of the fault after including the spatial rupture interactions. The theoretical proof of this is provided in Appendix A, and the empirical demonstration is shown later in the case study.

3.6 Parameter Estimation

The model has $2N + 1$ parameters: two for the BPT at each section (μ_j and α_j) and one for the correlogram (γ). Performing maximum likelihood estimation (MLE) over all the parameters requires constructing the expression for the joint likelihood of observing the rupture history at all sections of the fault and maximizing this expression to find the parameters' values. Because these procedures are complex, in this paper a simpler approach for parameter estimation is proposed. Instead of performing MLE over the $2N + 1$ parameters of the model, the approach is to 1) use MLE to estimate μ_j and α_j at each section separately, and then 2) calibrate γ in order to match the magnitude exceedance rates and the spatial distribution of the average seismic moment release from historical data. This procedure will be further shown in the case study. Ceferino et al. (2018a,b) provide additional methods for estimating the model parameters that use MLE and Bayesian updating.

Tweedie (1957) showed that the MLE estimators of μ_j and the variance σ_j^2 can be calculated as in Equations 10 and 11, respectively, where t_{jk} are the random samples of interarrival time $t_{j1}, t_{j2}, \ldots, t_{jn}$ in the j-th section, and n is the total number of samples. Then, $\hat{\alpha}_j$ can be estimated as $\hat{\sigma}_j / \hat{\mu}_j$. In case the number of samples is small, n can be replaced by $n - 1$ in Equation 11.

$$\hat{\mu}_j = \frac{1}{n} \sum_{k=1}^{n} t_{jk} \tag{10}$$

$$\hat{\sigma}_j^2 = \frac{1}{n} \sum_{k=1}^{n} \left(\frac{\hat{\mu}_j^3}{t_{jk}} - \hat{\mu}_j^2 \right) \tag{11}$$

4 Model application to the occurrence of large interface earthquakes near Lima, Peru

The model presented in this paper is used to analyze the rupture occurrence of large earthquakes and the associated seismic hazard at the interface (i.e., inter-slab region) of the subduction zone along the Coast of Lima, Peru. The interface surface is the contact area between the South American and Nazca Plates. Figure 4 shows the trench of the subduction zone parallel to the coastline. A detailed description of the tectonic features of this zone can be found in Villegas-Lanza et al. (2016).
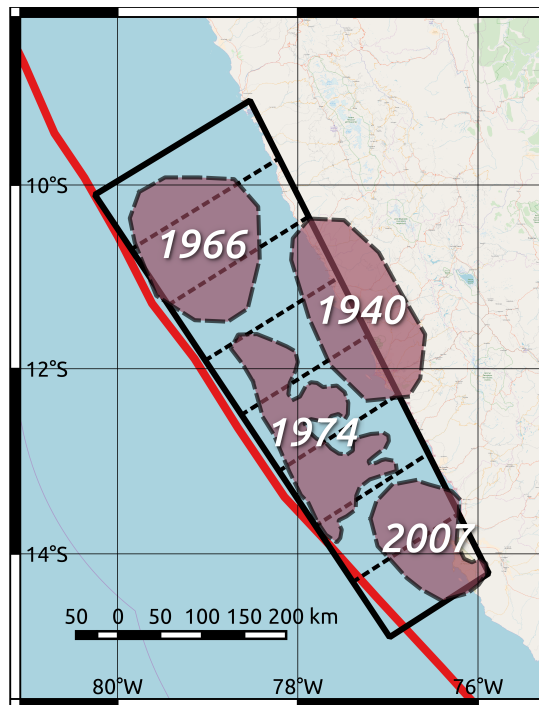

Figure 4: Subduction zone between the Nazca and South American plates. The line parallel to the coastline shows the fault trench, the black quadrilateral shows the region of study subdivided into eight sections, and the four enclosed areas show four earthquake rupture areas of past earthquakes with the year indicated in each area.

4.1 Earthquake data

Rupture data of large earthquakes occurring at the interface of the South American and Nazca Plates are used in this application. The geographic extent of the analysis includes the subduction zone region between the Nazca Ridge (South) and the Mendaña Fracture (North). No previous earthquake has ruptured through these boundaries, and geodetic data shows that there is creeping at these boundaries (i.e., slip locking is negligible, see Villegas-Lanza et al. (2016)). The region of analysis is shown by the large quadrilateral in Figure 4. The length along the strike direction is approximately 650 km, and the average width along the dip direction is 190 km. This region was divided into eight sections along the strike direction. Figure 4 shows the boundaries between the sections with dashed lines, where each section has a length of approximately 81.3 km.

Earthquake data for the region were collected from previous studies. The data contain the last 450 years of seismic activity and include the year of occurrence, the rupture location, and dimensions of earthquake events with magnitude larger than 7.5. Lower magnitudes were incomplete or unavailable for the 450 years, and therefore, they were not included in the analysis. Only interface events were included

in the dataset. Dorbath et al. (1990) estimated ruptures dimensions, locations, and magnitudes of earthquakes based on a collection of damage descriptions and isoseismal maps. The estimates in Dorbath et al. (1990) were used for earthquakes that occurred before 1940, prior to the installation of seismic recording stations. Data about earthquakes occurring after 1940 were collected from different sources, including (1) the rupture areas and locations of the 1940 and 1966 earthquakes estimated by Kelleher (1972), (2) the magnitudes of the 1940 and 1966 earthquakes estimated by Kanamori (1977), and (3) the rupture dimensions, locations, and magnitudes of the 1974 and 2007 earthquakes estimated by Langer and Spence (1995), and Chlieh et al. (2011), respectively. The geographic data of the earthquake rupture set were georeferenced and compiled in a geographic information system (GIS) file and are in a link in the Data and Resources section. Figure 4 shows the rupture areas of the 1966, 1940, 1974, and 2007 earthquakes. Table 1 shows list of total earthquakes and corresponding magnitudes in the historical catalog.

Table 1: Magnitude and occurrence year of historical earthquakes in the last 450 years.

Mw	Year	Mw	Year
8.1	1586	8.6	1746
7.5	1664	8.2	1940
7.85	1678	8.1	1966
8.4	1687	8.1	1974
7.5	1725	8.0	2007

The ruptures were projected along the trench of the subduction zone, allowing this case study to be represented in one dimension. Figure 5a shows the rupture projections along the strike direction over time from South to North. The ruptures lines were discretized and associated to individual sections of the fault. Rupture segments smaller than half of the sections' lengths were considered negligible. The resultant rupture lengths are shown in Figure 5b. Table 2 summarizes the 450-year catalog and shows the interarrival times and the time since the last rupture at each section of the fault.
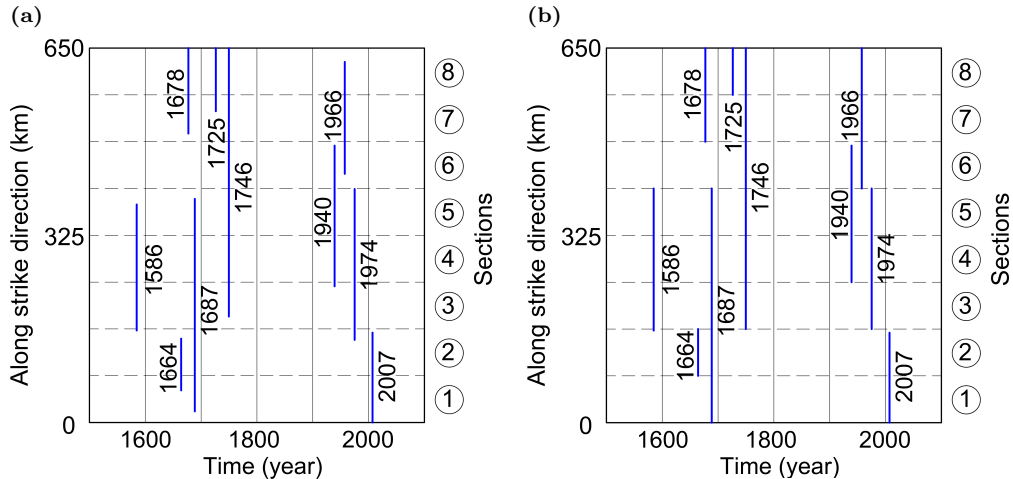

Figure 5: Projections of earthquake ruptures to the trench of the subduction zones over time: (a) estimated rupture lengths, (b) discretized rupture lengths

4.2 Parameter estimation

The 450-year catalog was used to estimate the 17 parameters of the model (i.e., μ_j and α_j in each section and γ). As described previously, the parameter estimation is performed in a two-step process. First, the BPT parameters μ_j and α_j at each section are evaluated, and then, the correlation parameter is estimated. Other techniques for parameter estimation can be found in Ceferino et al. (2018a), and a

Table 2: Earthquake data and estimated parameters

	Section labels							
	1	2	3	4	5	6	7	8
Last rupture occ. (year)	2007	2007	1974	1974	1974	1966	1966	1966
Interarrival times (years)	320	320	228	34	34	26	220	220
		23	59	194	194	194	68	21
			101	59	59			47
				101	101			
μ (years) (MLE)		172	129	97	97	110	144	96
α (MLE)		1.73	0.59	0.70	0.70	1.18	0.62	1.16

comparison of the effect of the parameter estimation technique selection on the seismic hazard can be found in Ceferino et al. (2018b)

4.2.1 Parameter estimation for individual sections:

The parameters μ_j and α_j are estimated at each fault section separately using Equations 10 and 11. Table 2 shows the estimated μ_j and α_j in each section. Because the sparsity of the data did not allowed a more reliable parameter estimation, two adjustments to the estimated parameters were made. The first adjustment was to the estimates of aperiodicity α_j (i.e., coefficient of variation) in sections 2, 6, and 8 of the fault. The estimates of aperiodicity α_2, α_6 and α_8 were considered unreliable since they were large compared to the aperiodicity in other sections and were particularly more sensitive to the data sparsity of our case study. Therefore, a value of 0.7 was assigned to the α_j of these three sections since 0.7 is closer to the values found in sections with more data points and is also closer to Bayesian estimates in a similar case study in the region (i.e., Ceferino et al. (2018b)). The second adjustment was to the estimates in section 1. The μ_1 and α_1 values of section 1 were assumed to be equal to those of section 2 because there were not enough data points in section 1 to perform parameter estimation.

Figure 6a shows the BPT distribution in black for sections 4 and 5 using the values of μ_j and α_j, calculated previously. Because all the ruptures in sections 4 and 5 occurred due to the same earthquake events, the interarrival data and the estimated parameters μ_j and α_j are the same for both sections. In addition, Figure 6a shows an exponential distribution with the equivalent mean of interarrival time in a lighter color. The exponential distributions of interarrival time are derived from the Poisson model and are used to model time-independent earthquake hazard. The graph shows that that the exponential distribution has higher probability of small interarrival times than the BPT distribution. The time-independent exponential model will be used later in the paper to provide comparisons with the presented model.

Figure 6b shows the annual rupture probability $p_t(j)$, as a function of $T_t(j)$, and the number of years since the last rupture at the j-th section, for fault sections 4 and 5 using the BPT and exponential interarrival time models. $p_t(j)$ was defined as the probability of occurrence of an event in the next one-year time increment given that there were $T_t(j)$ years without an earthquake in the section. Thus, $p_t(j)$ is equivalent to the definition of earthquake occurrence hazard rate for time increments of one year. Figure 6 shows that $p_t(j)$ starts from 0, increases up to a maximum point, and then flattens out in all the sections of the fault. Chhikara and Folks (1977) proved mathematically that for any value of μ_j and α_j, the rate $p_t(j)$ starts at 0, increase to a maximum value, and then decrease until reaching a constant asymptotic level. The BPT implies that an earthquake rupture at the j-th section immediately unloads all the stress at the corresponding location since the failure rate decreases to 0 after an event. The BPT also implies that the earthquake occurrence probability saturates to a constant value after a long seismic gap. This saturation suggests that, after a long period of time, all the additional tectonic stress is released through creep or other means. Although such a saturation has not been corroborated from empirical observations, it remains a major consequence of the BPT model. Figure 6b also shows the time-independent rupture probability rates resulting from the equivalent exponential pdf shown in Figure 6a. It can be seen that after an earthquake, the BPT rates start estimating rupture probabilities below the time-independent estimation. Then, because the time-independent rate remains constant over time, the BPT rates increase to higher probability levels. This feature is key to explaining the differences

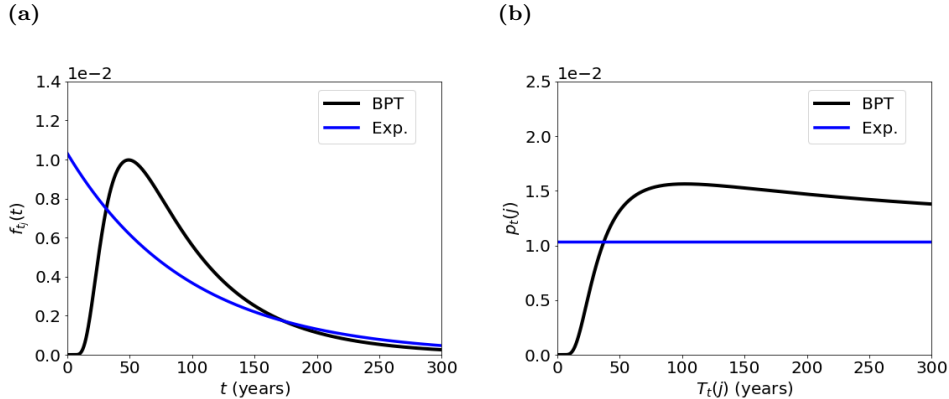between thee time-dependent and independent estimations of seismic hazard in Lima.

Figure 6: BPT in sections 4 and 5 in black and exponential with equivalent mean in lighter color: (a) probability density function, (b) hazard rate.

4.2.2 Parameter estimation for the correlogram

The parameter γ is calibrated for the exponential and the spherical correlation models. Multiple realizations of rupture occurrence were sampled using different values of γ. In this calibration, rupture occurrences in a 500,000-year interval were analyzed. The scaling equations for interface subduction-zone earthquakes, proposed by Strasser et al. (2010), were used to relate the rupture length in the sections to earthquake magnitude. Although the rupture length to magnitude relationship was treated as deterministic, the uncertainty in this relationship can be incorporated in the model. The model can generate a maximum earthquake magnitude of 8.8 as a result of the simultaneous rupture of all the sections (i.e., rupture length of 650 km). The annual magnitude exceedance rates and the average annual seismic moment release were calculated using these realizations for multiple values of γ. Additionally, magnitude exceedance rates and seismic moment releases were computed using the historical catalog in Figure 5. The γ values that generated occurrences closely matching the results from the historical data were selected. The scripts used for the calibration procedure are provided in a link the Data and Resources section.

The exponential correlation model in Equation 7 was tested using multiple γ values. This paper describes the results for γ values equal to 600, 900, 1,200, 1,500, and 1,800 km. Figure 7a shows a snapshot of the first 1,500 years of rupture simulation for γ equal to 1,200 km. The X axis represents the years of earthquake occurrence, and the Y axis represents the distance along the strike direction form South to North. The past earthquake observations are shown in black, and the simulated ruptures are shown in a lighter color.
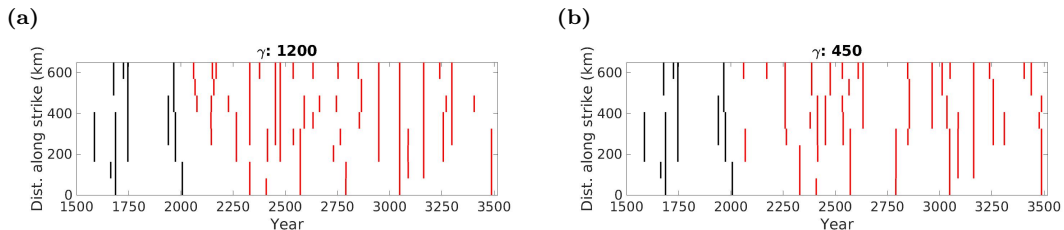

Figure 7: 1500-year rupture simulation (γ values are in km): (a) exponential correlogram, (b) spherical correlogram.

Figure 8a shows the exponential correlogram for the five values of γ with a lighter color. The graph shows the distance between the sections in the X axis and the correlation between two sections in the Y

13

axis. The correlation starts at 1 when the distance is 0 km, and it decreases as a function of distance. Larger values of γ correspond to slower decreases of the correlation and, therefore, sustained strong correlations at larger distances. Note that the correlogram is used to model the correlation on the Z_t vector (from the copulas approximation) and not the correlation on the X_t rupture vector. Therefore, the exponential correlogram does not match the correlations on X_t. In this paper, the correlations on Z_t are referred to as "apparent" correlations, whereas the correlations on X_t are referred to as "effective" correlations. To analyze the effective correlations, the rupture correlations of section $X_t(1)$ with each of the other sections were calculated using the 500,000-year simulations. The effective correlations are shown in black in Figure 8a for each of the γ values. The contrast between the apparent and effective correlation show that the copula method reduces the correlation values from the correlogram. Although the difference between the apparent and effective values of correlation does not change the selection of the γ value, it is important to note that the final rupture correlations introduced to the model are smaller than the values of the exponential correlogram. Further studies will analyze the relationship between the probabilities of rupture and the apparent and effective correlation values.
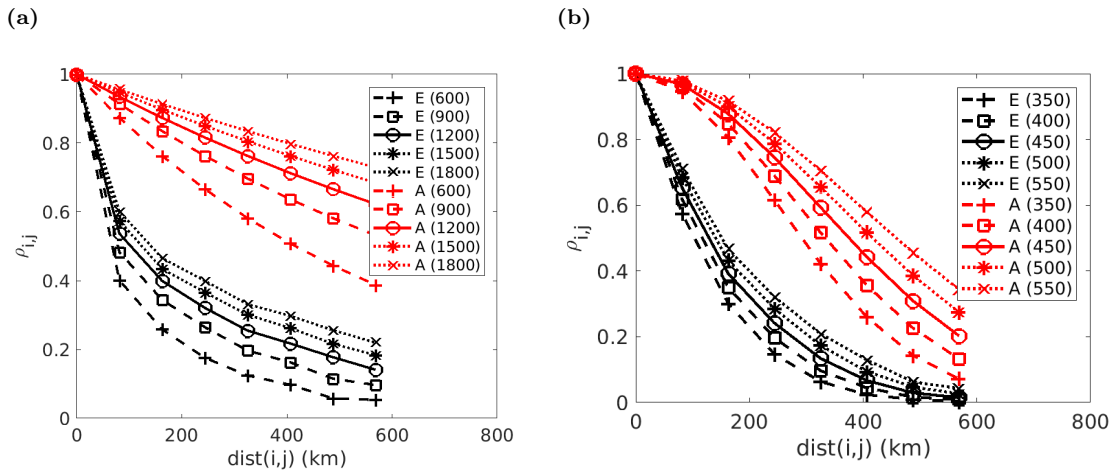

Figure 8: Apparent (A) and effective (E) correlations using different γ values (in parenthesis in km): (a) exponential correlogram, (b) spherical correlogram

The red lines in Figure 9a depict the annual magnitude exceedance rates resulting from the 500,000 years of rupture simulation using the exponential correlogram with the five γ values shown in Figure 8a. Figure 9a also shows the magnitude exceedance rates from the earthquake catalog. The results of the five γ values show a good match to the exceedance rates from the empirical data for magnitudes between 7.5 and 8.4. The model outputs fast-decreasing rates for larger magnitudes. As mentioned previously, the maximum magnitude was considered to be 8.8 as the result of a rupture over the eight fault sections. The catalog has only one earthquake larger than 8.4 (i.e., only the 1746 Mw 8.6 earthquake). Therefore, conclusive comparisons of empirical Mw rates with the model beyond Mw 8.4 are not possible. Larger values of γ increase the rates of large earthquakes because high γ values generate stronger effective correlations and therefore higher likelihood of rupturing multiple sections simultaneously.

The lighter lines in Figure 9b depict the average yearly release of seismic moment in the sections of the fault for the five values of γ. The average release obtained from the earthquake data is shown by the solid black line. Higher γ's had larger associated average moment release because γ makes more likely the occurrence of larger earthquakes. Though the rates from all different values of γ gave comparable results, γ equal to 1,200 km gave the best match.

The spherical correlation model in Equation 8 was also tested using multiple γ values. This paper shows the results for γ values equal to 350, 400, 450, 500, and 550 km because they provided good match to earthquake data. Figure 7a shows a snapshot of the first 1,500 years of rupture simulation for γ equal to 450 km.

Figure 8b shows with a lighter model the spherical correlation model for the five γ values. Larger
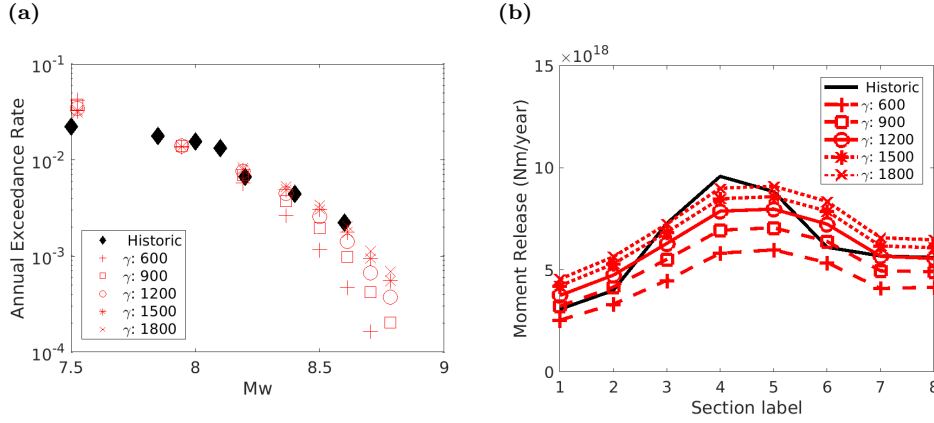
Figure 9: Model benchmark for different exponential correlograms: (a) Magnitude exceedance rates, (b) Average seismic moment (Nm/year)

values of γ correspond to higher values of correlation. In addition, the correlation decreases as a function of distance at faster rates than for the exponential correlogram. Similar to the case of the exponential correlogram, the spherical correlogram does not show the effective correlation values of the rupture vector because the copulas method is used. The effective correlations of the rupture in section $X_t(1)$ and the ruptures in each of the other sections were calculated from the 500,000-year simulation. The effective correlations are shown in black in Figure 8b for each of the γ values. The effective correlations from the spherical correlogram also decrease at large distances at a faster rate than the effective correlations from the exponential correlogram, as represented by the different kinds of black lines in Figures 8a and 8b.

The lighter lines in Figure 10a depict the annual exceedance rates resulting from the 500,000-year simulation with the spherical correlogram using the five γ values shown in Figure 8b. The black dots show the exceedance rates corresponding to the earthquake catalog. All the five γ values also show a good match to the exceedance rates from the empirical data for magnitudes between 7.5 and 8.4. The annual rates for large magnitudes saturate at a faster rate than when using the exponential correlogram because the spherical correlogram only sustains smaller effective correlations at large distances, as shown in Figure 8.

Figure 10b shows the average annual release of seismic moment for the five values of γ in lighter color. The black, solid line represents the average release obtained from the earthquake data. There is a direct relation between larger values of γ and larger releases of seismic moment. A γ equal to 450 km gave the results that best approximate the moments obtained from the earthquake data.
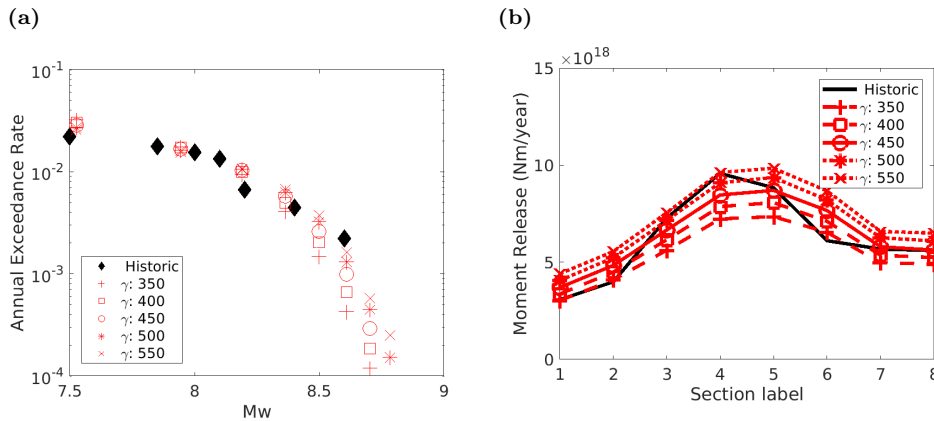

Figure 10: Model benchmark for different spherical correlograms: (a) Magnitude exceedance rates, (b) Average seismic moment (Nm/year)

In summary, both the exponential and spherical correlograms closely match both the magnitude exceedance rates and the annual seismic moment. The best fit to the data with the exponential correlogram was achieved with a γ value of 1,400 km, and the best fit to the data with the spherical correlogram was achieved with a γ value of 450 km.

4.3 Empirical model consistency

The model was next tested for consistency. For the model to be consistent, the initially assumed BPT distribution at each section should match the interarrival distribution resulting from the simulation process, after including the spatial interactions among multiple sections. The mathematical proof of model consistency is provided in Appendix A. Here, the empirical results showing consistency in section 4 are displayed in Figure 11. The back curve shows the initial BPT as defined in section 4 (i.e., $\mu_4 = 97$ and $\alpha_4 = 0.7$), and the bars depict the normalized histogram of rupture interarrivals resulting from the 500,000 years of simulation. The 5,064 ruptures occurred in section 4 during the simulation. As the plot shows, the simulation confirms that the histogram approaches the initial BPT distribution of section 4. The same procedure was applied to the other fault sections, and the results confirm that the histograms approached the respective BPT distributions in all the other fault sections. Therefore, the empirical results demonstrate that the model has consistency.
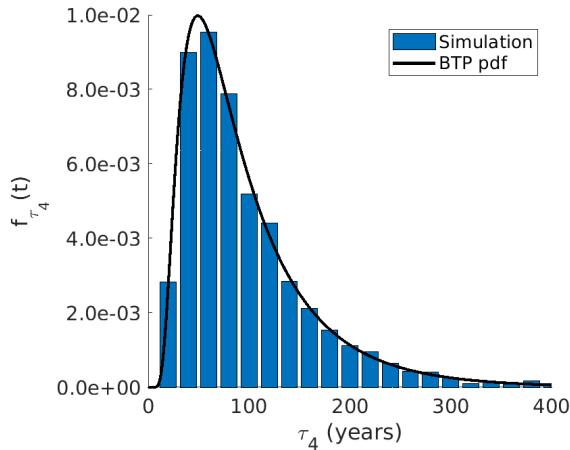

Figure 11: Proof of empirical consistency. BPT pdf in section 4: Initially assumed vs. simulation after including spatial interactions.

4.4 Comparison of time-dependent and independent hazards

This model was also used to estimate the time-dependent seismic hazard in the region and to compare the results with the time-independent seismic hazard. The spherical correlogram with γ equal to 500 km was used in the hazard assessment because it matches well the annual exceedance rates and seismic moment releases of the earthquake data, as stated previously. The hazard analysis includes only the contribution of magnitudes larger than 7.5 in the tectonic region. Abrahamson et al. (2016) developed a ground motion prediction equation (GMPE) for interface earthquakes in subduction zones. This GMPE was used to estimate peak ground accelerations (PGA) in the region. The hazard was calculated using OpenQuake software (Silva et al. (2014)), assuming a soil type B (Vs30 = 760 m/s) through the entire region of analysis.

The time-independent hazard was estimated using a Gutenberg Richter (GR) fit to the earthquake data, depicted by the black dots in Figures 9a and 10a. The resulting annual exceedance rate equation is $\nu_{M_w} = 10^{5.63 - 0.95 M_w}$. As mentioned previously, the minimum Mw was taken as 7.5, and the maximum as 8.8, which is equivalent to the rupture of all the eight sections in the fault. Additionally, the probabilities of earthquake occurrence were considered uniform over the tectonic region of analysis, which is represented by the in black polygon in Figure 12. Figure 12a shows the time-independent probabilities of

exceeding 0.4g of PGA in 30 years. Two features are notable from the graph. First, the hazard decreases with distance from the tectonic region because the ground shaking attenuates with distance from the rupture. Second, the time-independent seismic hazard close to the mid zone of the tectonic region is larger than the hazard close to the northern and southern boundaries. Site locations near the middle of the fault zone are exposed to larger number of events than those near the ends of the fault. The mid zone is exposed to strong shaking from mid- and large-size earthquakes that originate at both the northern and southern boundaries, whereas, say, the southern end of the fault is exposed to weak shaking from earthquakes originating at the northern end.

To estimate the time-dependent hazard, a Monte-Carlo simulation was performed on the model. The probabilities of earthquake occurrence during the next 30 years were estimated by analyzing every feasible rupture in sections of the fault model. Because the fault model has eight sections, there are 36 feasible earthquake ruptures: eight events rupturing single sections, seven rupturing two adjacent sections, six rupturing three adjacent sections, and so on. In general, the number of feasible earthquakes can be estimated as $N \times (N+1)/2$. For each feasible earthquake, the shaking distribution was calculated according to the GMPE by Abrahamson et al. (2016). The probabilities of exceeding a PGA of 0.4g during the next 30 years (from 2018 to 2047) were estimated over the region using both the probabilities of earthquake occurrence from the Monte Carlo simulation and the respective shaking distributions. Figure 12b shows the ratio between the resulting time-dependent probabilities and those from the time-independent analysis (Figure 12a). It can be seen that the time-independent results are higher than those from the time-dependent model in most of the region of analysis (i.e., where the ratio is below one). The time-independent results were particularly higher in the southern region, where the ratio values were even below 50%. The time-dependent hazard predicts smaller rupture probabilities in the southern zone because it incorporates in the analysis the recent release of energy caused by the 2007 earthquake, which ruptured the two southernmost sections of the tectonic region. As shown in Figure 6b, the sections reset their probability of rupture immediately after an earthquake in the time-dependent analysis, whereas such a probability remains constant in the time-independent analysis.

To assess the effect of the seismic gaps on the hazard, the probability of exceeding a PGA of 0.4g from 2048 to 2077 was calculated with the assumption that the seismic gap is extended for 30 years. This assessment is equivalent to a what-if analysis that assumes that there will no be earthquake occurrences from 2018 to 2047 in the tectonic region. Figure 12c shows the ratio between these time-dependent probabilities and those from the time-independent analysis. The comparison between Figures 12b and 12c shows how the hazard grows as the "seismic gap" increases. In the northern zone, the time-dependent hazard is larger than the time-independent hazard as a result of the stress accumulation during the additional 30-year seismic gap. The increase in the hazard in the whole fault is driven by the increase of rupture probability in each individual sections. Once the rupture probabilities of the sections exceed the one of the exponential, as shown in Figure 6b, the time-dependent hazard of the tectonic fault system will start exceeding the time-independent hazard.

Figure 12d shows the ratio of time-dependent to independent hazard probabilities after including additional 30 years of seismic gap (i.e., the hazard is calculated from 2078 to 2107 assuming no earthquakes from 2018 to 2077). It can be seen that the hazard keeps increasing in the region. Most of the northern region has 25% more predicted hazard than the time-independent hazard. Because of the BPT distribution, the probabilities of rupture occurrence at individual sections reach a constant plateau after long seismic gaps. After including the additional 30 years of seismic gap, most of the sections were close to their respective plateaus. For example, sections 4 and 5 were analyzed in the time interval between 104 and 134 years because the last rupture in those sections was in 1974. Figure 6b shows that the rupture probability is practically the same in this time interval. Most of the sections are close to their respective plateaus; therefore, the regional hazard shown in Figure 12d is approximately at the plateau of the time-dependent hazard in the region.

Additionally, the results showed that the differences between the time-dependent and independent hazard can be particularly sensitive at long distances. As represented by the darkest shade in Figure 12d, the mid region at approximately 150 km from the tectonic fault has ratios between 125% and 150%. At large distances, the seismic hazard is mainly driven by the effect of large earthquakes (i.e., rupture of multiple sections). The smaller earthquakes are not likely to generate PGA values larger than 0.4g at large distances because the shaking attenuates with distance at a fast rate. A similar trend can also be
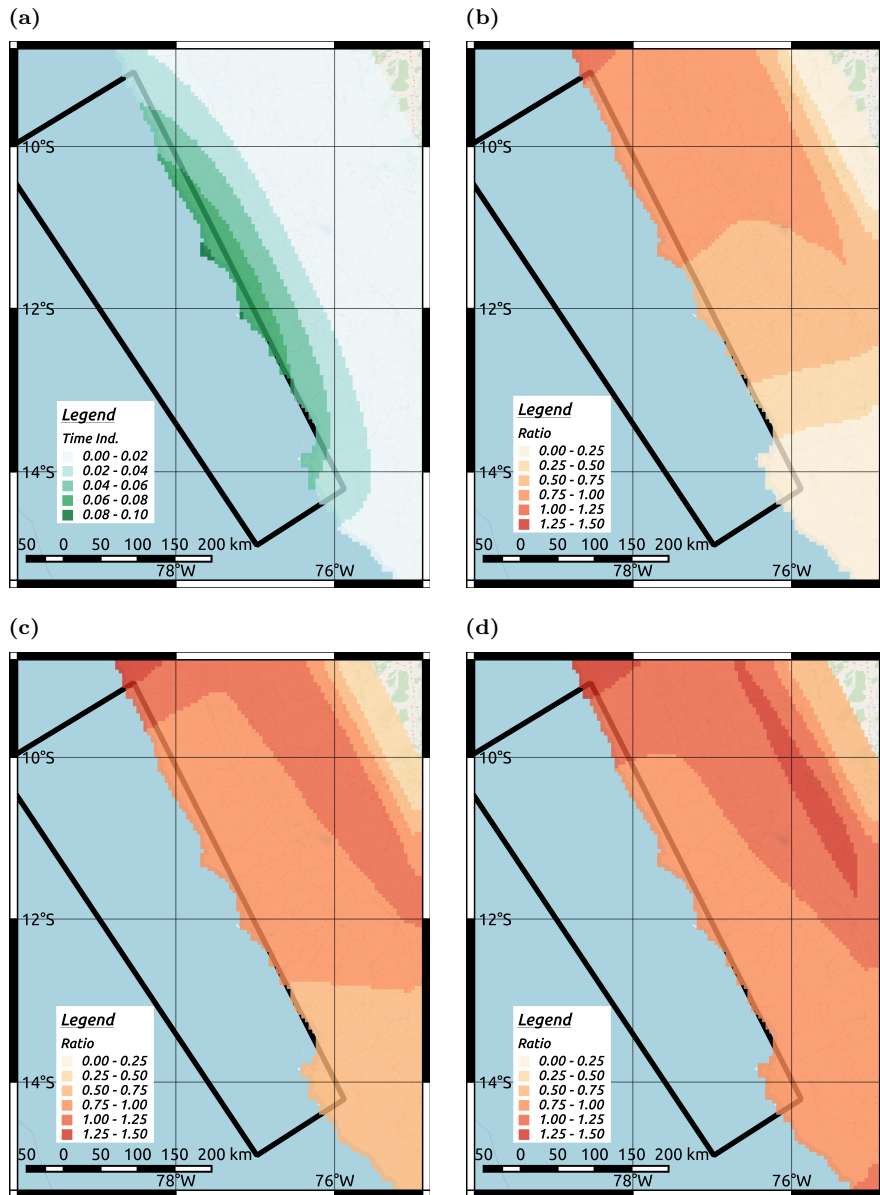
Figure 12: Comparison of P[PGA>0.4g] during 30 years: (a) time independent, (b), time dependent from 2018 to 2047 (c) time dependent with 30 extra years of seismic gap, (d) time dependent with 60 extra years of seismic gap.

18

seen in Figure 12c.

In summary, the hazard comparison shows that the model captures seismic gap effects and that such effects can have a significant effect on the seismic hazard of a region. Depending on the seismic gap in the region, the time-dependent hazard can be either higher or lower than the time-independent hazard. The results from this case study show that the time-dependent hazard for the next 30 years is up to 25% smaller than the time-independent hazard prediction in the mid and northern zones of the region; however, in the southern region, where a recent earthquake occurred, the 30-year time-dependent hazard can be up to a fourth of the time-independent hazard.

5   Conclusions

This paper has presented a novel probabilistic formulation for modeling the space and time interactions of earthquake mainshocks in tectonic faults. The formulation (1) idealizes a tectonic fault area as a two-dimensional surface, (2) discretizes the surface into small sections, and (3) models rupture occurrence of the section system as a correlated, multivariate Bernoulli process. The formulation models rupture occurrence of individual sections as Brownian passage-time (BPT) distributions, which are able to capture time-dependency of rupture occurrence (i.e., longer seismic gaps can increase the likelihood of rupture occurrence). A correlation model is also introduced to represent spatial interdependencies of rupture occurrences among the section of the fault, which represents the process of earthquake nucleation and rupture propagation among neighboring sections of the fault.

The model presented here is a suitable alternative for estimating seismic hazard to both probabilistic and physics-based existing models. Although physics-based models successfully capture complex features of rupture behavior, the uncertainty in the model parameters and the heavy computational demands make these models unsuitable for full seismic hazard calculations. In contrast, while current probabilistic models do not capture as many complex features of rupture behavior, their simplicity and smaller computation demands enable them to be extensively used in seismic hazard calculations. Thus, the proposed formulation is probabilistic and advances other existing probabilistic methods because it (1) captures time and space interactions of mainshocks that current smoothed seismicity models do not, (2) preserves the marginal distribution of interarrival times after including the spatial rupture interaction in multiple sections (i.e., model consistency), and (3) has an implicit physical interpretation consistent with current modern earthquake rupture behavior theories. This paper has provided both an empirical and mathematical proof for model consistency, as well as a simple approach for parameter estimation.

A case study demonstrating the applicability of the model presented here has also been provided. The study evaluated the rupture occurrence of large interface earthquakes in the subduction zone along the Coast of Lima, Peru. The data contain earthquakes with magnitudes larger than 7.5 that occurred during the last 450 years in the region. The results show that the correlograms can be successfully adjusted and that the model can replicate fairly well the annual exceedance rates of magnitude occurrence and the spatial variations of average seismic moment release. The results also show that the exponential correlograms generate higher probabilities of large magnitudes than the spherical correlograms because exponential correlograms preserve higher correlations for more distant fault sections. The model was also used to calculate time-dependent seismic hazard resulting from the large ruptures in the earthquake data. The probability of peak ground accelerations (PGA) larger than 0.4g during 30 years was estimated in the region. The results demonstrate that the time-dependent hazard was able to capture the spatial variations of earthquake events. Such variations are driven by the different mean interarrival times in the fault sections and the locations of recent earthquakes. The seismic gap effects modify the hazard to either lower of higher values than the Poissonian time-independent hazard according to how short or long the seismic gap is, respectively. It this model, the seismic hazard reaches an asymptotic constant value for long seismic gaps. In the application to Lima, the seismic gap effects decrease the seismic hazard during the next 30 years by up to 25% in the mid and northern regions. In the southern regions, where a more recent earthquake has occurred, the seismic hazard was reduced to up to a fourth of the time-independent seismic hazard.

Future studies will (1) propose more robust model parameter estimation techniques and include both synthetic physics-based and historical catalogs as model data, (2) study the relationship between prob-

ability of rupture and apparent and effective correlation of the copulas method, and (3) use anisotropic correlation models to incorporate variabilities of earthquake occurrence along the strike and dip directions.

6   Data and Resources

The data and resources in this paper was subdivided in two folders in this link `https://purl.stanford.edu/fk828tc8567`. In the first folder, "Previous ruptures in GIS", the rupture areas of the earthquakes in 1940, 1966, 1974, and 2007 are provided in a GIS format. The boundaries of the tectonic region of analysis shown in black in Figure 4 are also provided in GIS format. In the second folder "Scripts", Matlab scripts to reproduce the rupture simulation are provided.

7   Acknowledgments

References

Abrahamson, N., Gregor, N., and Addo, K. (2016). BC hydro ground motion prediction equations for subduction earthquakes. *Earthquake Spectra*, 32(1):23–44.

Anagnos, T. and Kiremidjian, A. S. (1984). Stochastic Time-predictable Model for Earthquake Occurrences. *Bulletin of the Seismological Society of America*, 74(6):2593–2611.

Barbot, S., Lapusta, N., and Avouac, J.-p. (2012). Under the Hood of the Earthquake Machine: Toward Predictive Modeling of the Seismic Cylce: Supplementary Material. *Science*, 336(May):1–20.

Ceferino, L., Galvez, P., Ampuero, J.-P., Kiremidjian, A., and Deierlein, G. (2018a). Bayesian Updating of Earthquake Rupture Model using Historic and Synthetic Physics-based Earthquake Catalogs. *Bulletin of the Seismological Society of America*, In Preparation.

Ceferino, L., Kiremidjian, A., and Deierlein, G. (2017). Space and time interaction modeling of earthquake rupture occurrence. In *ICOSAAR*.

Ceferino, L., Kiremidjian, A., and Deierlein, G. (2018b). Parameter Estimation Methods for Modeling of Time and Space Interactions of Earthquake Rupture. In *16th European Conference on Earthquake Engineering*, Thessaloniki.

Chhikara, A. R. S. and Folks, J. L. (1977). The Inverse Gaussian Distribution as a Lifetime Model. *Technometrics*, 19(4):461–468.

Chlieh, M., Perfettini, H., Tavera, H., Avouac, J. P., Remy, D., Nocquet, J. M., Rolandone, F., Bondoux, F., Gabalda, G., and Bonvalot, S. (2011). Interseismic coupling and seismic potential along the Central Andes subduction zone. *Journal of Geophysical Research: Solid Earth*, 116(12):1–21.

Dieterich, J. (1994). A constitutive law for rate of earthquake its application to earthquake clustering production and Haberman , Alternate assumptions to (2) might be. *Journal of Geophysical Research: Solid Earth*, 99(B2):2601–2618.

Dieterich, J. H. (1979). Modeling of rock friction: 1. Experimental results and constituve equations. *Journal of geophysical research*, 84(9):2161–2168.

Dorbath, L., Cisternas, A., and Dorbath, C. (1990). Assessment of the size of large and great historical earthquakes in Peru. *Bulletin of the Seismological Society of America*, 80(3):551–576.

Ellsworth, W. L. and Beroza, G. C. (1995). Seismic Evidence for an Earthquake Nucleation. *SCIENCE-NEW YORK THEN WASHINGTON*, pages 851–851.

Field, E. H. (2015). Computing Elastic-Rebound-Motivated Earthquake Probabilities in Unsegmented Fault Models: A New Methodology Supported by Physics-Based Simulators. *Bulletin of the Seismological Society of America*, 105(2A):544–559.

Field, E. H. and Gupta, V. (2008). Conditional, Time-dependent probabilities for segmented Type-A faults in the WGCEP UCERF 2, Appendix N in The Uniform California Earthquake Rupture Forecast, version 2 (UCERF 2): U.S. Geological Survey Open-File Report 2007-1437N and California Geological. Technical report, United States Geological Survey, Pasadena, CA.

Galvez, P., Ampuero, J. P., Dalguer, L. A., Somala, S. N., and Nissen-Meyer, T. (2014). Dynamic earthquake rupture modelled with an unstructured 3-D spectral element method applied to the 2011 M9 Tohoku earthquake. *Geophysical Journal International*, 198(2):1222–1240.

Hagiwara, Y. (1974). Probability of earthquake occurrence as obtained from a Weibull distribution analysis of crustal strain. *Tectonophysics*, 23(3):313–318.

Helmstetter, A. and Werner, M. J. (2014). Adaptive smoothing of seismicity in time, space, and magnitude for time-dependent earthquake forecasts for California. *Bulletin of the Seismological Society of America*, 104(2):809–822.

Jin, R., Wang, S., Yan, F., and Zhu, J. (2015). Generating Spatial Correlated Binary Data Through a Copulas Method. 3(4):206–212.

Kagan, Y. Y. and Jackson, D. D. (2014). Statistical earthquake focal mechanism forecasts. *Geophysical Journal International*, 197(1):620–629.

Kagan, Y. Y. and Jackson, D. D. (2015). Likelihood analysis of earthquake focal mechanism distributions. *Geophysical Journal International*, 201(3):1409–1415.

Kagan, Y. Y. and Knopoff, L. (1987). Random stress and earthquake statistics: spatial dependence. *Geophysical Journal International*, 88(3):723–731.

Kanamori, H. (1977). The energy release in great earthquakes. *Journal of Geophysical Research*, 82(20):2981.

Kelleher, J. a. (1972). Rupture zones of large South American earthquakes and some predictions. *Journal of Geophysical Research*, 77(11):2087.

Kiremidjian, A. S. and Anagnos, T. (1984). Stochastic Slip-predictable Model for Earthquake Occurrances. *Bulletin of the Seismological Society of America*, 74(2):739–755.

Langer, C. and Spence, W. (1995). The 1974 Peru Earthquake Series. *Bulletin of the Seismological Society of America*, 85(3):665–687.

Lohman, R. B. and McGuire, J. J. (2007). Earthquake swarms driven by aseismic creep in the Salton Trough, California. *Journal of Geophysical Research: Solid Earth*, 112(4):1–10.

Luo, Y., Ampuero, J. P., Miyakoshi, K., and Irikura, K. (2017). Surface Rupture Effects on Earthquake Moment-Area Scaling Relations. *Pure and Applied Geophysics*, 174(9):3331–3342.

Lutz, K. A. and Kiremidjian, A. S. (1995). A Stochastic Model for Spatially and Temporally Dependent Earthquakes. *Bulletin of the Seismological Society of America*, 85(4):1177–1189.

Marone, C. (1998). Laboratory-Derived Friction Laws and Their Application To Seismic Faulting. *Annual Review of Earth and Planetary Sciences*, 26(1):643–696.

Marsan, D. and Lengliné, O. (2008). Extending earthquakes'reach through cascading. *Science*, 319(5866):1076–1079.

Matthews, M. V., Ellsworth, W. L., and Reasenberg, P. a. (2002). A Brownian model for recurrent earthquakes. *Bulletin of the Seismological Society of America*, 92(6):2233–2250.

Nishenko, S. and Buland, R. (1987). A generic recurrence interval distribution for earthquake forecasting. *Bulletin of the Seismological Society of America*, 77(4):1382–1399.

Ogata, Y. (1988). Statistical models for earthquake occurrences and residual analysis for point processes.

Petersen, M. D., Moschetti, M. P., Powers, P. M., Mueller, C. S., Haller, K. M., Frankel, A. D., Zeng, Y., Rezaeian, S., Harmsen, S. C., Boyd, O. S., Field, N., Chen, R., Rukstales, K. S., Luco, N., Wheeler, R. L., Williams, R. A., and Olsen, A. H. (2014). Documentation for the 2014 Update of the National Seismic Hazard Maps. Technical report, USGS.

Reid, H. F. (1911). The Elastic-Rebound Theory of Earthquakes. *Bulletin of the Department of Geology, University of California Publications*, vol. 6, no:413–444.

Richards-Dinger, K. and Dieterich, J. H. (2012). RSQSim Earthquake Simulator. *Seismological Research Letters*, 83(6):983–990.

Rikitake, T. (1974). Probability of Earthquake Occurrence as Estimated from Crustal Strain. *Tectonophysics*, 23:299–312.

Ruina, A. (1983). Slip instability and state variable friction laws. *Journal of Geophysical Research: Solid Earth*, 88(B12):10359–10370.

Savage, J. C. and Langbein, J. (2008). Postearthquake relaxation after the 2004 M6 Parkfield, California, earthquake and rate-and-state friction. *Journal of Geophysical Research: Solid Earth*, 113(10):1–17.

Schwartz, D. P. and Coppersmith, K. J. (1984). Fault behavior and characteristic earthquakes: Examples from the Wasatch and San Andreas Fault Zones. *Journal of Geophysical Research: Solid Earth*, 89(B7):5681–5698.

Silva, V., Crowley, H., Pagani, M., Monelli, D., and Pinho, R. (2014). Development of the OpenQuake engine, the Global Earthquake Model's open-source software for seismic risk assessment. *Natural Hazards*, 72(3):1409–1427.

Strader, A. and Jackson, D. D. (2014). Near-prospective test of Coulomb stress triggering. *Journal of Geophysical Research: Solid Earth RESEARCH*, 119:3064–3075.

Strader, A., Jackson, D. D., Hardebol, N. J., Maier, C., Nick, H., Geiger, S., Bertotti, G., Boro, H., Behn, M. D., Grove, T. L., Strader, A., Jackson, D. D., Behn, M. D., Grove, T. L., Strader, A., Jackson, D. D., Hardebol, N. J., Maier, C., Nick, H., Geiger, S., Bertotti, G., and Boro, H. (2015). Journal of Geophysical Research : Solid Earth. *Journal of Geophysical Research: Solid Earth*, 120:1667–1676.

Strasser, F. O., Arango, M., and Bommer, J. J. (2010). Scaling of the Source Dimensions of Interface and Intraslab Subduction-zone Earthquakes with Moment Magnitude. *Seismological Research Letters*, 81(6):951–954.

Tweedie, M. C. K. (1957). Statistical Properties of Inverse Gaussian Distribution I. *The Annals of Mathematical Statistics*, 28(2):362–377.

Udias, A. and Rice, J. (1975). Statistical analysis of microearthquake activity near San Andreas geophysical observatory, Hollister, California. *Bulletin of the Seismological Society of America*, 65(4):809–827.

Villegas-Lanza, J. C., Chlieh, M., Cavalié, O., Tavera, H., Baby, P., Chire-Chira, J., and Nocquet, J.-M. (2016). Active tectonics of Peru: Heterogeneous interseismic coupling along the Nazca megathrust, rigid motion of the Peruvian Sliver, and Subandean shortening accomodation. *Journal of Geophysical Research : Solid Earth*, pages 1–24.

Wesnousky, S. G. (1994). The Gutenberg-Richter or characteristic earthquake distribution, which is it? *Bulletin of the Seismological Society of America*, 84(6):1940–1959.

Appendixes

A Proof of consistency of the model

The proof for model consistency is provided here. Consistency is shown by demonstrating that the interarrival time preserves its initial BPT distribution at any section when the model spatial interactions are included. It will be shown that the CDF of the BPT distribution will be preserved at each integer year because the model was also presented for discrete year-based time intervals. A similar proof can be derived for any other time intervals. Without loss of generality, it is considered that the j-th section experienced a rupture at year $y = 0$ (i.e., $X_j(0) = 1$). The next interarrival time τ_j will be smaller than Y years if and only if there is at least one rupture in the section during the following Y years. This event set is equivalent to the union of events consisting of having the next first rupture at each possible year between 1 and Y (i.e., $X_j(y) = 1, X_j(y - 1) = 0, X_j(y - 2) = 0, X_j(y - 3) = 0, \ldots, X_j(1) = 0$, for any $1 \leq y \leq Y$). Therefore, the equality shown in Equation A1 holds.

$$P[\tau_j \leq Y] = P[\cup_{y=1}^{Y} \left(X_j(y) = 1, X_j(y - 1) = 0, \ldots X_j(1) = 0 | X_j(0) = 1 \right)] \tag{A1}$$

Because elements of the event set are mutually exclusive, then, the probability of the union can be assessed as the sum of probabilities shown in Equation A2.

$$P[\tau_j \leq Y] = \sum_{y=1}^{Y} P[X_j(y) = 1, X_j(y - 1) = 0, \ldots X_j(1) = 0 | X_j(0) = 1] \tag{A2}$$

Additionally, $X_j(0) = 1$ is equivalent to $\tau_j(1) = 1$ since a rupture resets the time since the last earthquake. Therefore, adding $\tau_j(1)$ to the conditioning set does not change the final results as shown in Equation A3a. Furthermore, each event in the sum of Equation A2 represents the probability of the next rupture occurring during year y. This is equivalent to the event: $\{\tau_j(1) = 1, \tau_j(2) = 2, \ldots, \tau_j(y) = y, \tau_j(y + 1) = 1\}$. Since both events are equivalent, then Equation A3b holds.

$$P[\tau_j \leq Y] = \sum_{y=1}^{Y} P[X_j(y) = 1, X_j(y - 1) = 0, \ldots, X_j(1) = 0 | X_j(0) = 1, \tau_j(1) = 1] \tag{A3a}$$

$$P[\tau_j \leq Y] = \sum_{y=1}^{Y} P[\tau_j(y + 1) = 1, X_j(y) = 1, \tau_j(y) = y, X_j(y - 1) = 0, \tau_j(y - 1) = y - 1, \ldots, \tag{A3b}$$
$$X_j(1) = 0, \tau_j(1) = 1 | X_j(0) = 1, \tau_j(1) = 1]$$

In addition, the set $\{T_{y+1}(j), X_y(j)\}$ is a Markov chain because it is independent of all the previous rupture history conditioned on the last step $\{T_y(j), X_{y-1}(j)\}$. This is because $\{T_y(j), X_{y-1}(j)\}$ contains all the required information to assess the probability of rupture in the section during the next year. Then, Equation A3b can be rewritten into Equation A4.

$$P[\tau_j \leq Y] = \sum_{y=1}^{Y} P[X_j(y) = 1, \tau_j(y + 1) = 0 | X_j(h - 1) = 0, T(y) = y] \times \tag{A4a}$$
$$P[X_j(y - 1) = 0, \tau_j(y) = h | X_j(y - 2) = 0, \tau_j(y - 1) = y - 1] \times \ldots$$
$$P[X_j(1) = 0, \tau_j(2) = 2 | X_j(0) = 1, \tau_j(1) = 1]$$

Next, T_{y+1} is dropped from the event $\{\tau_j(y+1), X_j(y) | X_j(y-1), \tau_j(y)\}$ since $\tau_j(y+1)$ and $X_j(y)$ are equivalent events given the conditional term. $X_j(h - 1)$ is also dropped from the conditional probability since the $\tau_j(y)$ is the only information that is needed to evaluate the likelihood of $X_j(y)$ (Equation 2). Then, Equation A5 holds.

$$P[\tau_j \leq Y] = \sum_{y=1}^{Y} P[X_j(y) = 1 | \tau_j(y) = y] \times P[X_j(y - 1) = 0 | \tau_j(y - 1) = y - 1] \times \ldots \tag{A5a}$$
$$P[X_j(2) = 0 | \tau_j(2) = 2] \times P[X_j(1) = 0 | \tau_j(1) = 1]$$

25

Equation A5 shows that the earthquake occurrence likelihood at section j can be calculated as the sum of rupture probabilities at consecutive year intervals. It also shows that this probability can be calculated independently of the spatial rupture interactions with neighboring sections. Therefore, the correlogram introduced in the model does not change the final marginal distribution of the intearrival time at section j. The multiplicand $P[X_j(y) = 1|\tau_j(y) = y]$ in Equation A5 represents the the probability of having a rupture during year y at section j given that there was no rupture during the last $y-1$ years. Thus, this multiplicand is equivalent to the probability that the interarrival time random variable τ_j at section j is less than or equal to y given that τ_j is greater than $y-1$ (i.e., $\tau_j \leq y|\tau_j > y-1$). Similarly, the multiplicand $P[X_j(y-1) = 0|\tau_j(y) = y-1]$ is equivalent to $P[\tau_j > y-1|\tau_j > y-2]$ because $X_j(y-1) = 0$ means that there is no rupture during year $y-1$. Using the same logic, all the multiplicands of Equation A5 were replaced by their equivalences as a function of τ_j as shown in Equation A6a. Then, using the Bayes's rule, the conditional probabilities in Equation A6a were rewritten as shown in Equation A6b. Note that the multiplication in Equation A6b simplifies to the expression in Equation A6c since the denominator equals the numerator of the next term and $P[\tau_j \leq 0]$ is 0. $F(y)$ equals $P[\tau_j \leq y]$ and is the BPT CDF (Equation 5). Finally, the first term of the y summand cancels out with the second term of the $y+1$ summand. It can be seen that the final expression is equivalent to the BPT CDF and that the model preserves the interarrival time distribution. Therefore, the model is consistent.

$$P[\tau_j \leq Y] = \sum_{h=1}^{Y} P[\tau_j \leq y|\tau_j > y-1] \times P[\tau_j > y-1|\tau_j > y-2] \times \ldots P[\tau_j > 2|\tau_j > 1] \qquad \text{(A6a)}$$
$$\times P[\tau_j > 1|\tau_j > 0]$$

$$P[\tau_j \leq Y] = \sum_{h=1}^{Y} \frac{P[y-1 < \tau_j \leq y]}{1 - P[\tau_j \leq y-1]} \times \frac{1 - P[\tau_j \leq y-1]}{1 - P[\tau_j \leq y-2]} \times \cdots \frac{1 - P[\tau_j \leq 2]}{1 - P[\tau_j \leq 1]} \times \frac{1 - P[\tau_j \leq 1]}{1 - P[\tau_j \leq 0]} \qquad \text{(A6b)}$$

$$P[\tau_j \leq Y] = \sum_{y=1}^{Y} P[y-1 < \tau_j \leq y] = \sum_{y=1}^{Y} F_{\tau_j}(y) - F_{\tau_j}(y-1) = F_{\tau_j}(Y) - F_{\tau_j}(0) = F_{\tau_j}(Y) \qquad \text{(A6c)}$$